Servo Motor Characterization for Project Zephyrus

Connor Sterling

May 2026

1 Introduction

This report details the results of characterization experiments for the servo motor used on the MIT Rocket Team's Project Zephyrus. Before proceeding, the reader should familiarize themself with [1], the report on the servo characterization for the motors used on Project Xanthus, the demonstrator for and precursor to Zephyrus. This report will omit much of the background covered therein.

Section 2 provides a list of materials needed to conduct the experiments and Sections 3–4 describe the setup and test cases. Key results are presented in Section 5, while the majority of the data can be found in the appendices. Section 6 briefly concludes the report.

2 Equipment

The servos used on Zephyrus are the KST A12-T servo. They have coreless motors, steel gears, and contactless magnetic position sensors. The A12-T is a more robust model from the same supplier used for Xanthus. The specifications are found in Table 1 and an image in Fig. 1. See [2] for more information.

Table 1: KST A12-T specifications

Rated Voltage	DC7.4V
Voltage Range	DC6.0V-8.4V
Torque	1.6N.m@6.0V, 1.8N.m@7.4V, 2.0N.m@8.4V
Speed	0.15sec/60°@6.0V, 0.13sec/60°@7.4V, 0.12sec/60°@8.4V
Working Frequency	1520us/333Hz
Default Travel Angle ±60°	120°
Total Temperature Range	-10℃. . . +60℃
Soft Start	Yes
Programmable	Yes
Case Material	Aluminum Alloy
Motor Type	7 Phases Coreless DC Motor
Gear Set Material	Hardened Steel
Position Sensor	Contactless (Magnetic Sensor)
Ball Bearing	2BB
Case Dimensions	30mm*12mm*35.5mm±0.2mm
Weight	32g±10%

Hardware used for the experiment:

- KST A12-T servo
- AS5600 magnetic encoder [3]
- Cylindrical magnet (provided by Avionics subteam)
- Arduino Mega 2560

- Digilent Analog Discover 2 (AD2)
- Kungber SPS3010 0 30 V/0 10 A power supply
- Inertia simulation mass (ISM)
- 3 X M3x10mm bolt (spring mount)
- 2 X 17.30 lb/in extension spring
- 2 X 23.66 lb/in extension spring
- Encoder mount (PLA)
- Servo mount (aluminum)
- 2 X 1/4-20x3" bolt (spring mount)
- Baseplate (aluminum)

Figure 1: KST A12-T servo.

3 Experimental Setup

Initial experiments with non-metallic mounts proved suspect. Plastic and wood materials were too prone to deformation under the heavy loading required to simulate Zephyrus' flight conditions. Thus, the servo was mounted on an aluminum plate fixed at 90° to a thick aluminum baseplate. The tabs on Zephyrus are aluminum, and the same material was used for the ISM. Three radii were chosen to apply torque via the springs, and protruding M3 bolts were screwed into the ISM at these points. The magnet provided with the AS5600 was lost, and so a different cylindrical magnet was acquired from the Avionics subteam. This one was polarized differently, and so needed to be mounted on its curved surface. The magnetic encoder is positioned above the magnet via the 3D-printed encoder mount. See Figs. 2–4.

The spring constants chosen are 17.30 lb/in and 23.66 lb/in. The radii of the M3 spring mounts on the ISM are 0.75, 1.10, and 1.50 in from the servo's output drive. The springs are fixed to the baseplate via tall 1/4-20 bolts in line with the M3 mount. Fig. 5 is an abstract depiction of the configuration when the ISM is displaced to an angle α. Here, r is the radius of the M3 mount from the servo shaft $\boldsymbol{O}$, and L is the length of each spring under no rotation (N.B. while in theory the spring forces will cancel out at $\alpha = 0$, variations in k between springs with the same nominal rate may cause this assumption to fail).

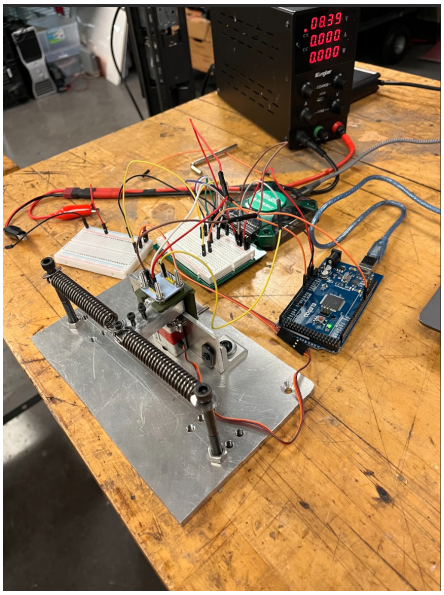

Figure 2: Experimental setup.

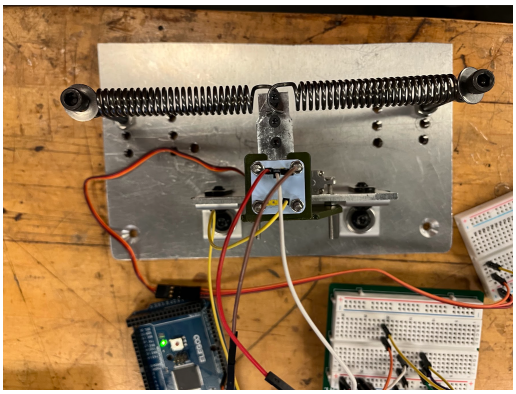

(a)

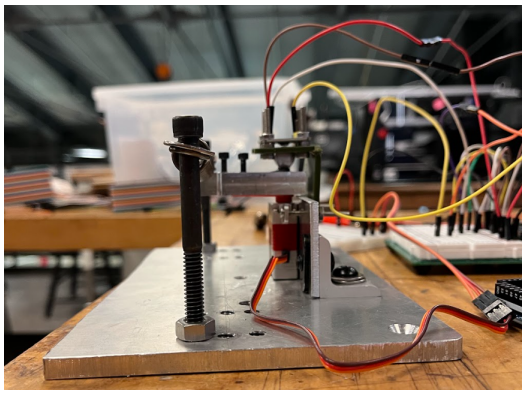

(b)

Figure 3: Experimental setup top and side views.

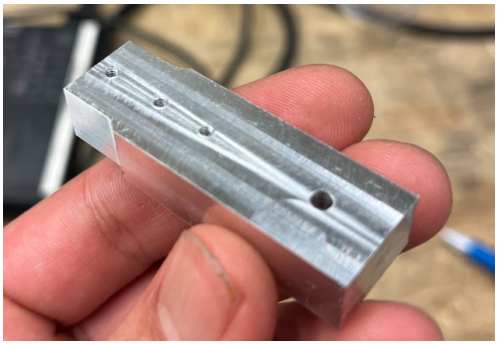

(a)

(b)

Figure 4: Inertia Simulation Mass.

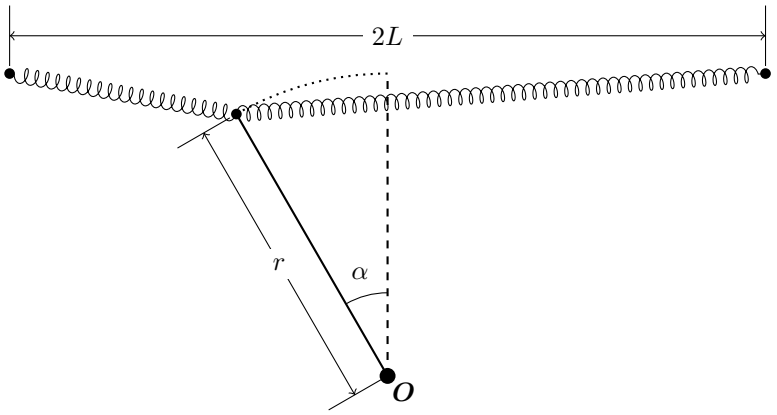

Figure 5: Experiment abstraction. The servo shaft is at O. The ISM is rotated from its neutral position by angle α. The distance from the servo shaft to spring connection is r, and each spring's length at equilibrium is L.

If the L is assumed to be the springs' unstrained length, it can be shown that the torque about $\boldsymbol{O}$ due to the spring in compression is

$$\tau_{comp} = k\ r \cos\left(\alpha + \arctan\left[\frac{r - r\cos\alpha}{L - r\sin\alpha}\right]\right)\left(\sqrt{(L - r\sin\alpha)^2 + (r - r\cos\alpha)^2} - L\right) \tag{1}$$

and is

$$\tau_{ext} = k\ r \cos\left(\alpha - \arctan\left[\frac{r - r\cos\alpha}{L + r\sin\alpha}\right]\right)\left(L - \sqrt{(L + r\sin\alpha)^2 + (r - r\cos\alpha)^2}\right) \tag{2}$$

for the spring in tension. Positive moment is defined as out of the page in Fig. 5, in the direction of positive α. The derivation of the above is left to the reader. Both equations 1 and 2 simplify to

$$\tau = -k\ r^2\alpha \tag{3}$$

under small angle approximation. Differentiating with respect to α and summing the torques yields the load rate that the experiment seeks to replicate:

$$\frac{d\tau}{d\alpha} = -2kr^2. \tag{4}$$

Let κ denote the load rate, where

$$\kappa \equiv \frac{d\tau}{d\alpha}. \tag{5}$$

The combination of spring constant and radius is then equated to the aerodynamic loading.

In reality, the assumption that L is the springs' unstrained length is not true. Extension springs are used, and they must be stretched when mounted, as they cannot be compressed beyond their unstrained length. For two springs with the same stiffness, though, the neutral point $\alpha = 0$ still corresponds to zero net torque, and $d\tau/d\alpha$ can still be calculated with Equation 4.

The servo angle command is sent from the AD2's W1 channel to Channel 1 and to the Arduino. An Arduino script maps W1 to a PWM signal corresponding to an angular range of -10° to 10° and sent to the servo. The encoder voltage output is sent to AD2 Channel 2. Bode plots are generated using the AD2's network analysis feature. The encoder is powered by the Arduino's 5 V output. The servo is powered at 8.39 V from the power supply to simulate the available voltage from the flight computer. Everything is on a common ground.

4 Test Matrix

Zephyrus' flight profile covers a broad range of aerodynamic regimes. Lift and moment coefficients, speed, and density all change throughout the flight. The load rate the servo must overcome depends on these quantities as

$$\frac{d\tau}{d\alpha} = C_{N\alpha}\ q\ S_{ref}\ r_L. \tag{6}$$

Here, $C_{N\alpha}$ is the change in normal force on the tab per unit actuation, S_{ref} is the area of the tab, q is dynamic pressure, and r_L is the lever arm from the servo shaft to the tab's center of lift. Five of the six possible spring/radius combinations are tested, as well as a no-load case. For each case, three frequency response trials are performed and results averaged. The frequency range is 1 Hz–20 Hz. In [1] it was shown that aliasing occurs above 22.5 Hz, and so higher frequency data would not be valuable. Variance between trials is negligible. Additionally, for each load case a steady-state response to ±5° and ±10° is tested to measure the achieved angle under load. Table 2 contains the test matrix.

Table 2: Test Matrix

Case	Spring Rate [N/mm]	Radius [cm]	Load Rate [N·m/rad]	Percent Max L.R. [%]
0	0.000	–	0.00	0.0
1	3.030	1.90	-2.19	24.8
2	4.144	1.90	-2.99	33.9
3	3.030	2.79	-4.72	53.3
4	4.144	2.79	-6.45	72.9
5	3.030	3.81	-8.80	99.2

5 Results and Analysis

5.1 Steady-State Response

First the steady-state responses will be discussed, as the results thereof inform the frequency response analysis. These trials consist of commanding the servo to either ±5° or ±10° for 5 seconds each. Unlike in [1], there is significant degradation in servo performance under the loads expected for Zephyrus' flight. This is manifested in a failure to reach the full commanded angle in steady state. This can be readily seen in the time series for the steady-state response of Case 5 (the maximum load case) shown in Fig. 6.

It is difficult to know *a priori* how loading affects the servo's achieved vs. commanded angle. One observation of interest is that the steady-state angle achieved, α_{ss}, does not necessarily correspond to stall. The motor is able to produce more torque, as evidenced by the fact that when the command angle, α^*, is increased, so too does α_{ss}. The fraction α_{ss}/α^* is essentially the same in both the 5° and 10° steady-state trials for a given load case. This type of behavior would seem to imply a lack of integral control in the servo's internal algorithm. These experiments suggest there is a linear attenuation in α_{ss}/α^* with loading, as evidenced by Fig. 7.

The steady-state angle can then be predicted from the command as a function of the load rate according to

$$\alpha_{ss} = \left(1 - p\ \frac{\kappa}{\kappa_0}\right)\ \alpha^*, \tag{7}$$

where p is the attenuation rate and κ_0 is the reference load rate, equal to the maximum load rate predicted on the flight. A linear regression of all cases yields $p = 0.438$. One would expect α_{ss}/α^* to decrease monotonically with the load rate. Suspiciously, though, there appear to be two different attenuation rates: one for the springs with stiffness 17.30 lb/in and one for the 23.66 lb/in springs. These stiffnesses were not measured, but taken as the nominal value. Future experimenters would do well to measure the spring rates for themselves.

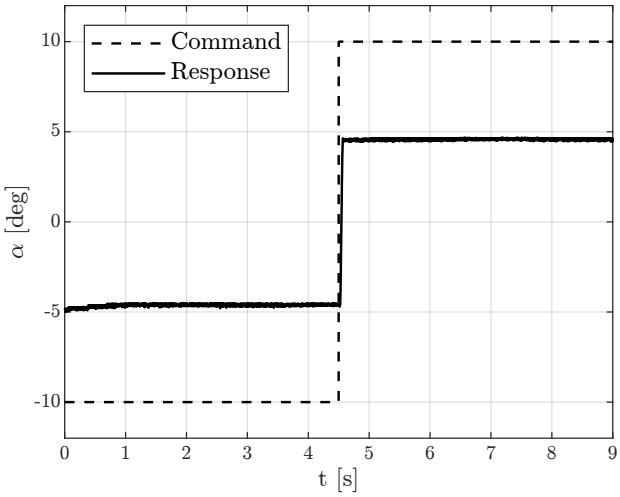

Figure 6: 10° steady-state response for Case 5. The servo is only able to achieve 49% the commanded range.

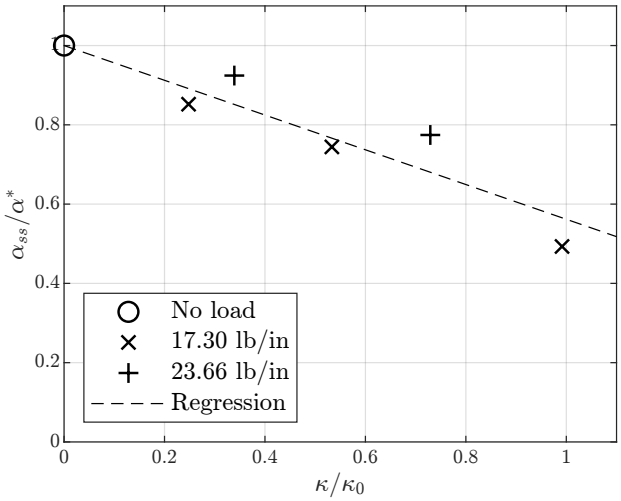

Figure 7: As the load rate is increased, the steady-state angle achieved for a given command decreases. Points represent the mean α_{ss}/α^* of the 5°and 10° trials. The attenuation rate of the regression line is 0.438.

5.2 Frequency Response

Recall from [1] that the goal of the frequency response trials is to determine a transfer function adequate to model the servo for controller design. The chosen form of the transfer function is

$$G_{servo}^{CL} = k_{att} \cdot \frac{b_2 s^2 + b_1 s + b_0}{a_3 s^3 + a_2 s^2 + a_1 s + a_0}. \tag{8}$$

Here, k_{att} is the load-dependent attenuation factor. This depends on the load case, and is equal to α_{ss}/α^* from Equation 7. The transfer function form is labelled "N3M2" in [1], with the addition of k_{att}.

Similar to [1], an unconstrained optimization is performed to find the coefficients a_0–a_3 and b_0–b_2. Once again, the constraint $a_0 = b_0$ is enforced. However, the objective function is not weighted by proximity to resonance, and is simply the squared error of the complex gains:

$$J = |G_{experimental} - G_{model}|^2. \tag{9}$$

The value of k_{att} is prescribed for a given load case using the results of the steady-state tests.

Fig. 8 plots the poles and zeros of the fitted transfer functions for all load cases. Clearly, there are imperfections, either in the experiment or the fitting. The zeros for case 4 (orange) are anomalous. Moreover, there is not a monotonic trend in the apparent root locus with load rate. This is consistent with the suspect results in the steady-state tests. Nevertheless, the implication of a trend does emerge, characterized by the slowing of the real pole and speeding up of the complex pole and zero pairs. The latter are suggestive of a second-order Padé approximation for a time delay:

$$e^{-sT} \approx \frac{\frac{T^2}{12}s^2 - \frac{T}{2} + 1}{\frac{T^2}{12}s^2 + \frac{T}{2} + 1}. \tag{10}$$

T is the delay in seconds. The fact that the delay diminishes with increasing load can be explained if the reduction in distance traveled (because $\alpha_{ss} < \alpha^*$) outweighs any decrease in speed.

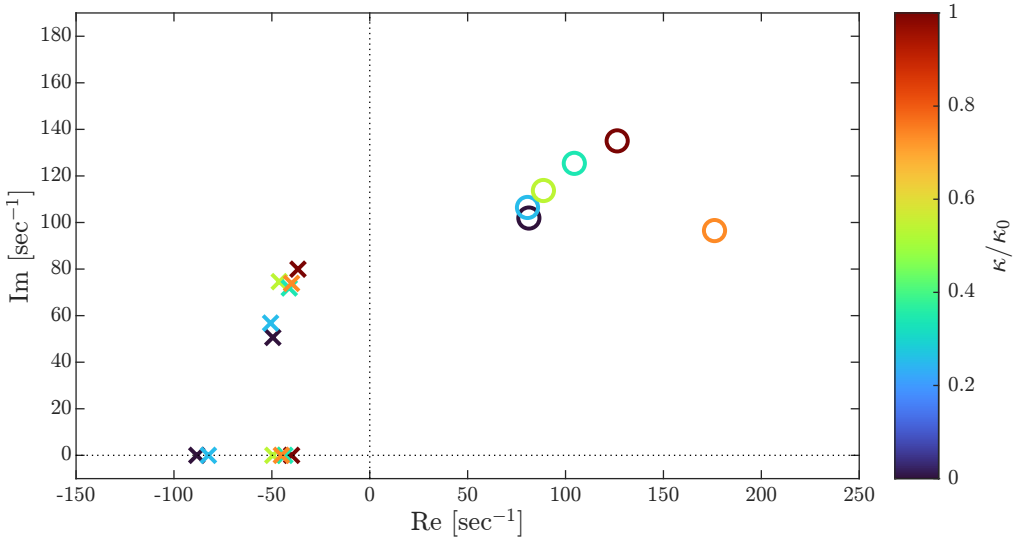

Figure 8: Pole-zero map for all load cases. The system's complex pole and zero pairs suggest a second order Padé approximation for a time delay. The delay decreases with load rate.

Fig. 9 displays the fitted frequency response curves for all load cases. The magnitude plot reflects the general decrease in steady state angle with load rate. The bandwidth of the system is around 9 Hz. The phase plots of all cases are remarkably similar. Divergence occurs as the frequency exceeds the system's bandwidth, with higher load cases exhibiting less phase loss. This reflects the locations of the complex poles and zeros explained above.

Tabulated coefficients and poles/zeros are available in appendix A. Bode plots for each case comparing the fitted transfer function with the experiments over a broader range of frequencies can be found in appendix B.

6 Conclusion

The purpose of these experiments was to determine a continuous time transfer function that could accurately represent the servo under flight conditions for the purpose of controller design. They were successful in that regard. Because there is minimal difference in phase below the bandwidth (and differences are benign with increasing load), the closed loop transfer function of the servo will be modeled as:

$$G^{CL}_{servo}(\kappa) = k_{att}(\kappa) \cdot G^{CL}_{servo}(\kappa = 0). \tag{11}$$

Thus, only k_{att} depends on the load rate, not the pole and zero locations. Fixing the pole and zero locations vastly simplifies the controller design. Essentially, the design is performed with $k_{att} = 1$, and when the

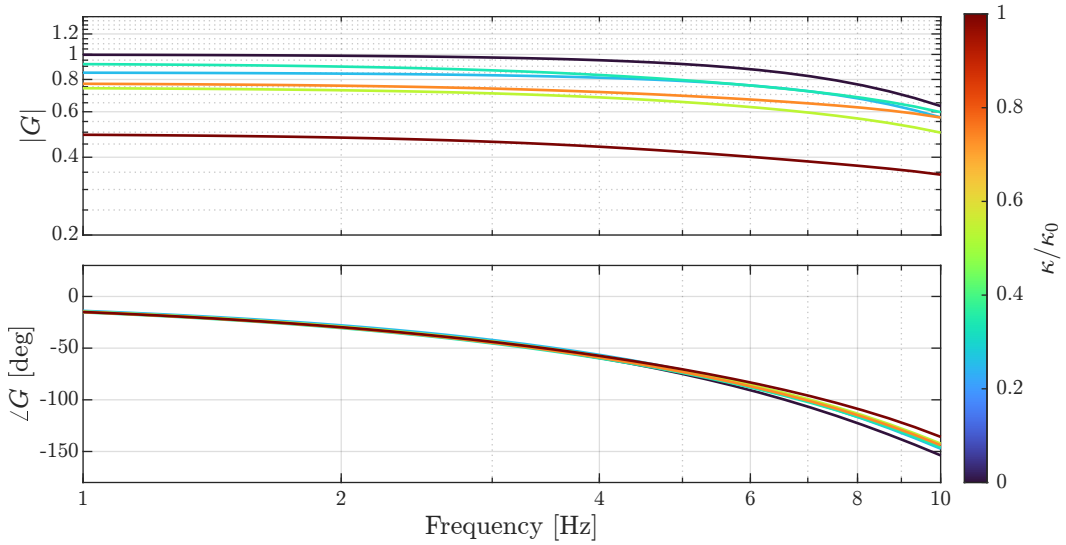

Figure 9: Bode plot overlay of all load cases. Phase loss is similar for all cases, while the magnitude decreases according to the attenuation rate.

control law is implemented, the command angle is multiplied by a factor of $1/k_{att}(\kappa)$ to account for the diminished α_{ss}.

To close this report, what follows are several pieces of advice for anyone seeking to replicate and improve upon these experiments:

- **Jig materials.** Use metals for any parts of the jig that are in the load path connected to the springs. For springs as stiff as the ones employed here, this is essential. Earlier iterations of the experiments used wood or plastics, resulting in significant deformations of the jig while the servo actuated.
- **Springs.** As commented earlier, measuring the spring rates experimentally would be wise. Relatively cheap springs from McMaster-Carr have sizeable tolerances on their stiffnesses. Error therein not only affects the calculation of κ, but if the two springs used do not have the same stiffness, $\alpha = 0$ will not be the neutral point for evenly spaced mounts.
- **Spring mounting bolts.** In an effort to combat the uncertainty in spring rates, the 1/4-20 mounting holes were drilled by hand on a drill press. The two springs to be used were attached to each other and stretched, and the mounting holes were drilled such that the meeting point of the springs was in line with the servo shaft. Measuring the stiffnesses would allow a more premeditated calculation of the hole locations, which could be done on a waterjet and thus much more precisely.
- **Spring attachment.** When attaching extension springs to the ISM (after the mounting bolts and outer ends of the spring are fixed to the baseplate), it is necessary to do so one at a time, stretching each spring in the process. In the intermediate step where only one spring is attached to the ISM, there is substantial torque which will cause the ISM to rotate towards the already attached spring. To prevent this, a short piece of 80/20 was mounted vertically to brace the ISM during this step, then removed once both springs were attached.
- **Magnet.** Glue the magnet in place to prevent it from slipping during experiments. Orient it in such a way to avoid 0°/360° wraparound discontinuities from the magnetic encoder.
- **Time.** Setting up and conducting these experiments never failed to take two or three times as long as anticipated. Plan accordingly.

A Tabulated coefficients, poles, and zeros

Table 3: Attenuation factor and fitted coefficients

Case	κ/κ_0	k_{att}	a_0	a_1	a_2	a_3	b_0	b_1	b_2
0	0.000	1.000	442234	13737.9	187.037	0.99833	442234	-4230.26	26.0258
1	0.248	0.852	442257	13101.7	170.220	0.92653	442257	-3997.78	24.8102
2	0.339	0.924	442178	15494.7	186.707	1.48643	442178	-3468.06	16.5964
3	0.533	0.744	442219	14243.6	164.675	1.16014	442219	-3770.73	21.2552
4	0.729	0.774	442199	14809.5	173.774	1.38981	442199	-3861.82	10.9655
5	0.992	0.493	442188	15269.7	162.155	1.43192	442188	-3266.75	12.9250
Mean	-	-	442213	14442.9	174.095	1.23220	442213	-3765.90	18.7630
S.D.	-	-	29.7816	923.018	10.7049	0.23777	29.7816	351.135	6.24669
R.S.D.	-	-	0.0067%	6.3908%	6.1489%	19.2967%	0.0067%	9.3241%	33.2926%

Table 4: Poles and zeros

Case	$p_{1,2}$	p_3	$z_{1,2}$
0	-49.50 ± 50.63j	-88.34	81.27 ± 101.92j
1	-50.65 ± 56.80j	-82.41	80.57 ± 106.46j
2	-41.11 ± 71.88j	-43.38	104.48 ± 125.41j
3	-46.23 ± 74.60j	-49.49	88.70 ± 113.74j
4	-39.95 ± 73.85j	-45.13	176.09 ± 96.53j
5	-36.67 ± 79.95j	-39.91	126.37 ± 135.06j
Mean	-44.02 ± 67.95j	-58.11	109.58 ± 113.19j
S.D.	5.14	6.04	36.17
R.S.D.	6.35%	10.40%	22.96%

B Bode plots comparing experiment to fitted models

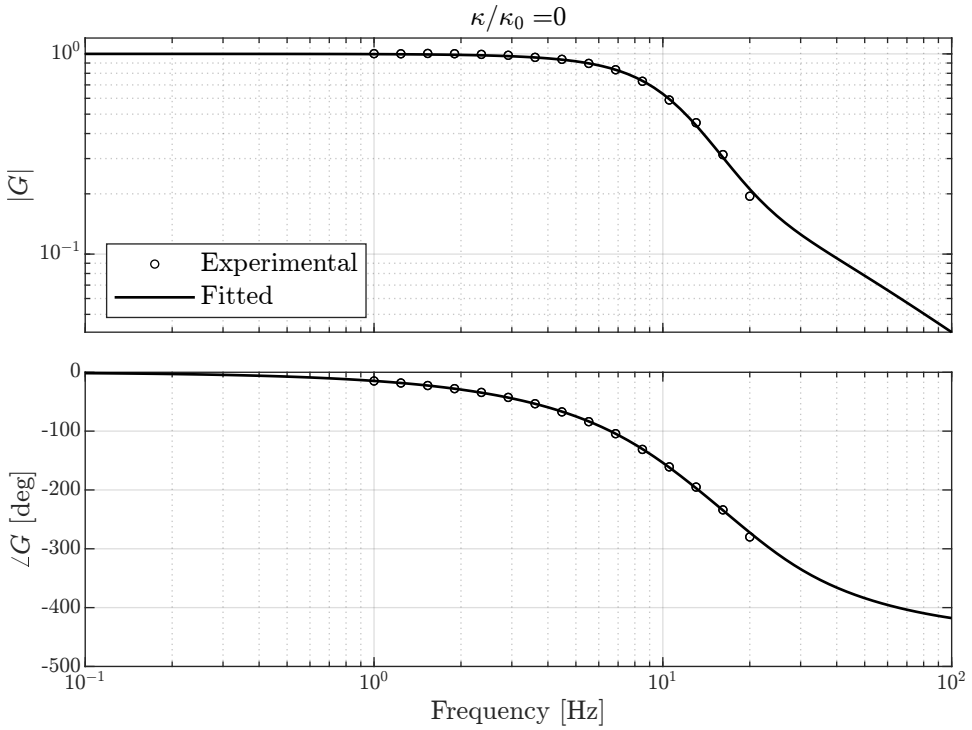

Figure 10: Case 0 Bode plot.

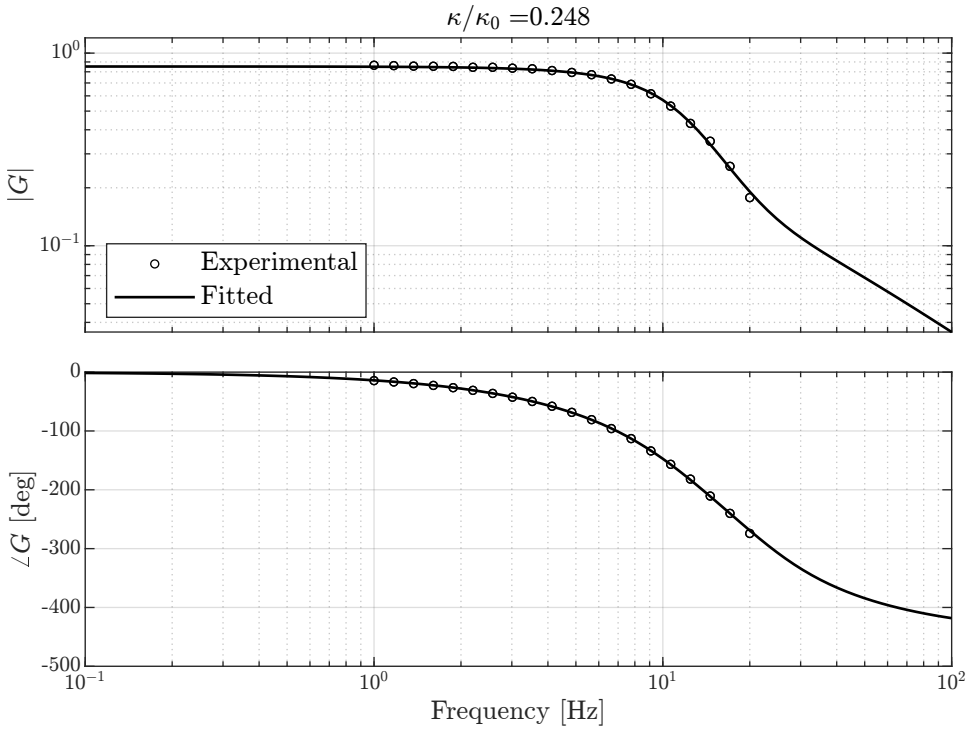

Figure 11: Case 1 Bode plot.

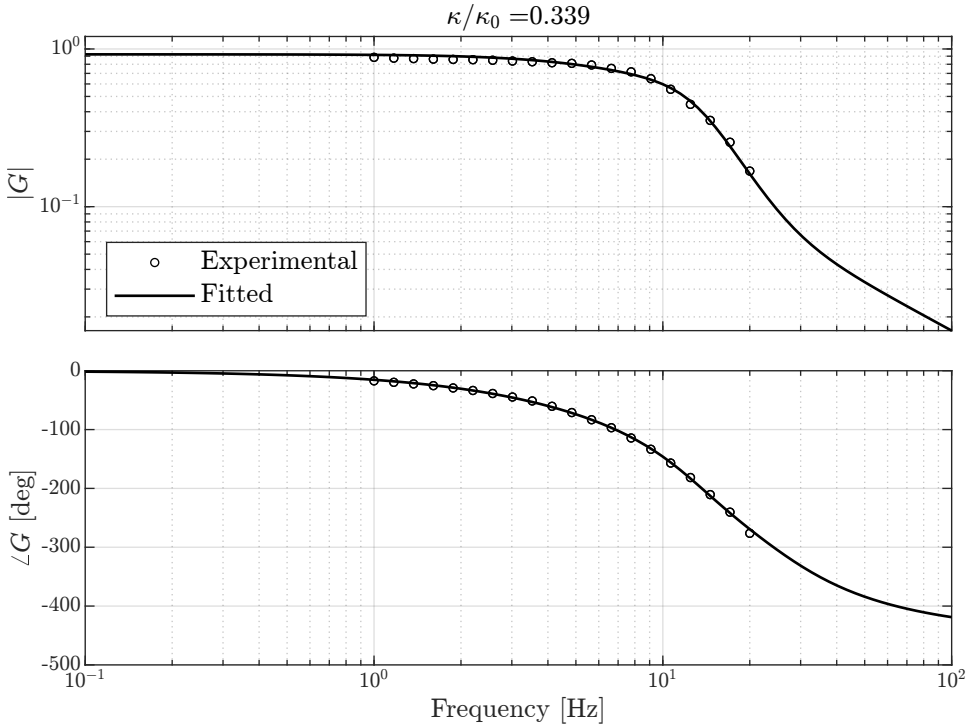

Figure 12: Case 2 Bode plot.

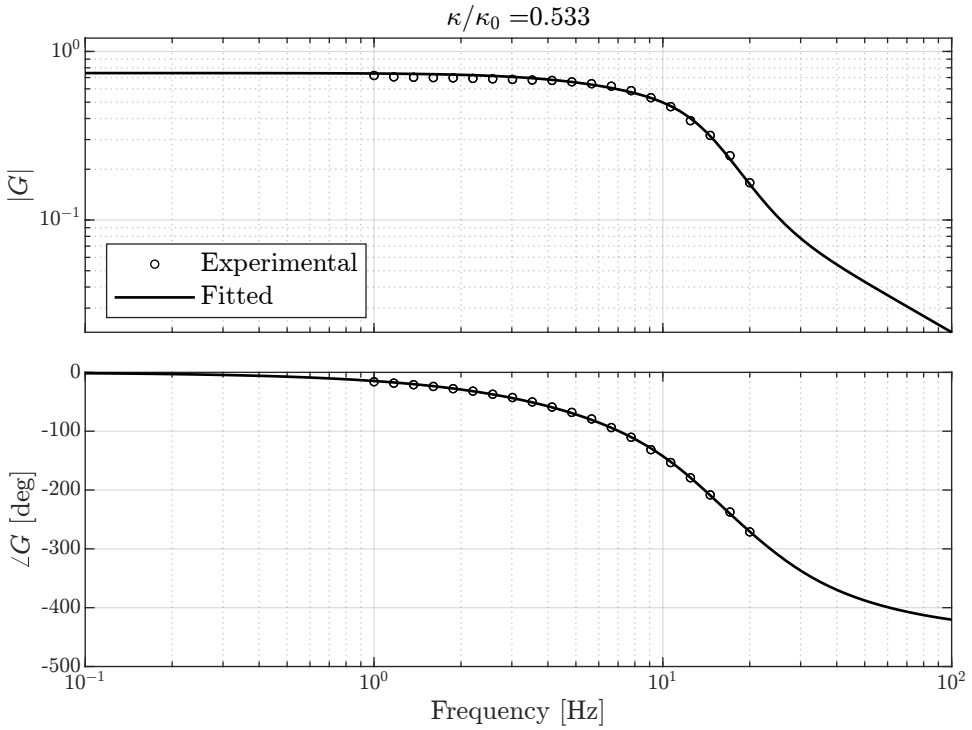

Figure 13: Case 3 Bode plot.

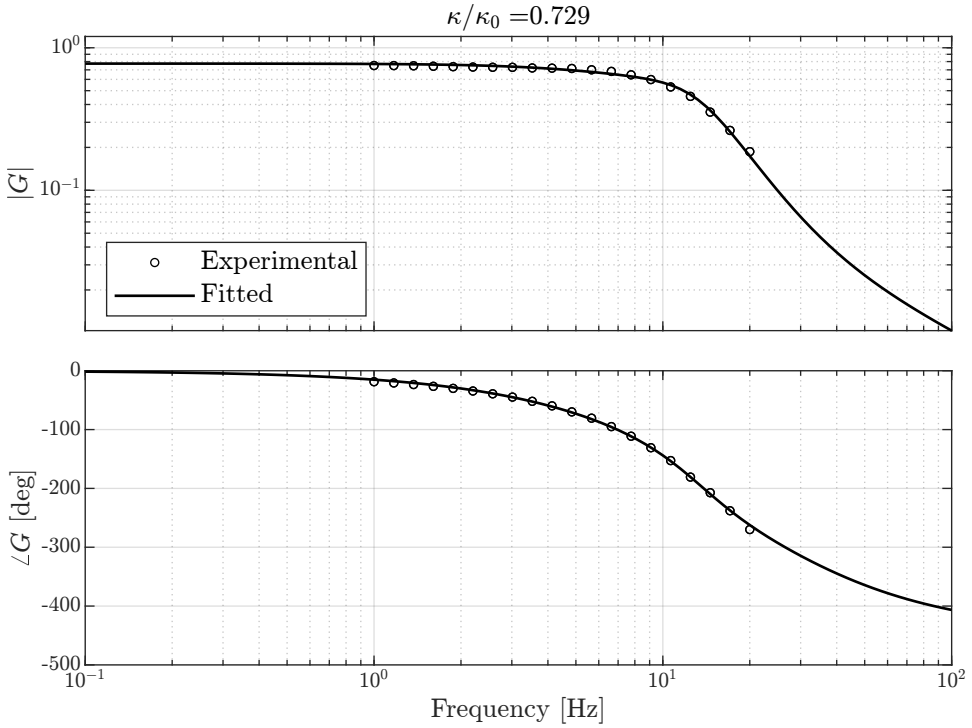

Figure 14: Case 4 Bode plot.

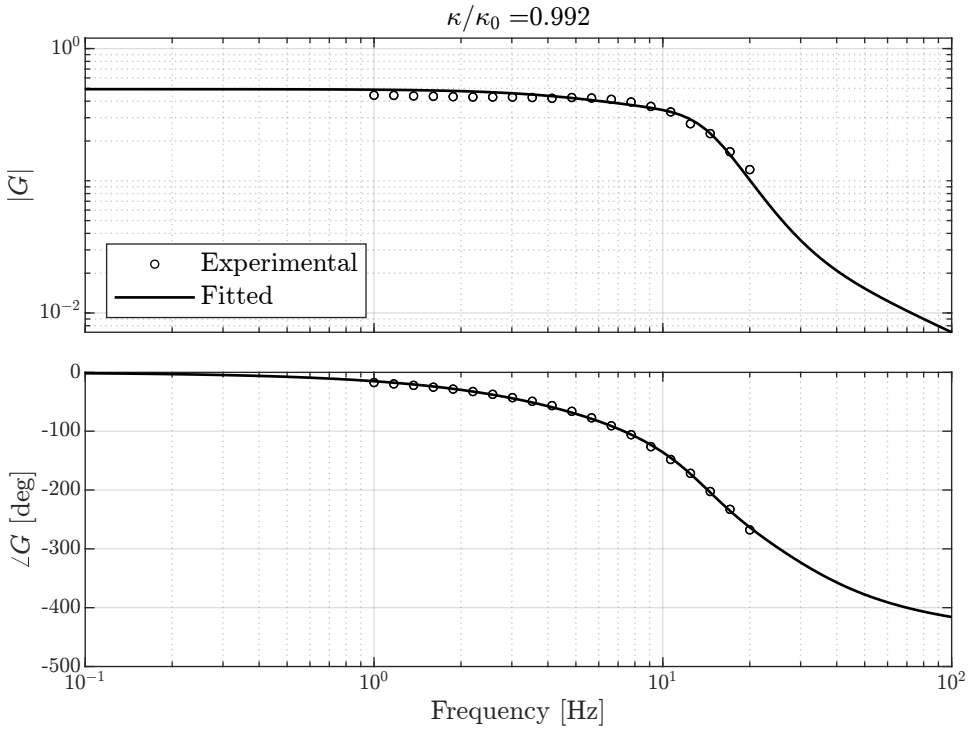

Figure 15: Case 5 Bode plot.

References

[1] C. Sterling, "Servo Motor Characterization for Project Xanthus," 2025.

[2] KST Servos, "X06 V6.0 HV Micro Digital Metal Gear Glider 1.8kg Torque Servo Motor," 2025, accessed: 2025-09-17. [Online]. Available: https://kstservos.com/products/x06-v6-0-hv-micro-digital-metal-gear-glider-1-8kg-torque-servo-motor

[3] AMS OSRAM, *AS5600 12-bit Programmable Contactless Potentiometer Operation Manual*, Dec. 2014, accessed: 2025-09-17. [Online]. Available: https://look.ams-osram.com/m/4f8342513a447495/original/AS5600_UG000254_2-00.pdf